Available online at www.sciencedirect.com

ScienceDirect

Geochimica et Cosmochimica Acta 159 (2015) 61–79

Geochimica et Cosmochimica Acta

www.elsevier.com/locate/gca

Interactions of arsenic with calcite surfaces revealed by in situ nanoscale imaging

François Renard [a,b,c,*], Christine V. Putnis [d,e], German Montes-Hernandez [a,b], Encarnacion Ruiz-Agudo [f], Jörn Hovelmann [d], Géraldine Sarret [a,b]

[a] Univ. Grenoble Alpes, ISTerre, BP 53, F-38041 Grenoble, France
[b] CNRS, ISTerre, BP 53, F-38041 Grenoble, France
[c] Physics of Geological Processes, University of Oslo, Norway
[d] Institut für Mineralogie, Universität Münster, Corrensstrasse 24, 48149 Münster, Germany
[e] Department of Chemistry, Curtin University, PO Box U1987, Perth, WA 6845, Australia
[f] Department of Mineralogy and Petrology, University of Granada, Fuentenueva s/n, 18071 Granada, Spain

Received 29 November 2014; accepted in revised form 21 March 2015; available online 27 March 2015

Abstract

Arsenic dissolved in water represents a key environmental and health challenge because several million people are under the threat of contamination. In calcareous environments calcite may play an important role in arsenic solubility and transfer in water. Arsenic–calcite interactions remain controversial, especially for $As^{(III)}$ which was proposed to be either incorporated as such, or as $As^{(V)}$ after oxidation. Here, we provide the first time-lapse in situ study of the evolution of the (10–14) calcite cleavage surface morphology during dissolution and growth in the presence of solutions with various amounts of $As^{(III)}$ or $As^{(V)}$ at room temperature and pH range 6–11 using a flow-through cell connected to an atomic force microscope (AFM). Reaction products were then characterized by Raman spectroscopy. In parallel, co-precipitation experiments with either $As^{(III)}$ or $As^{(V)}$ were performed in batch reactors, and the speciation of arsenic in the resulting solids was studied by X-ray absorption spectroscopy (XAS). For $As^{(V)}$, AFM results showed that it interacts strongly with the calcite surface, and XAS results showed that $As^{(V)}$ was mostly incorporated in the calcite structure. For $As^{(III)}$, AFM results showed much less impact on calcite growth and dissolution and less incorporation was observed. This was confirmed by XAS results that indicate that $As^{(III)}$ was partly oxidized into $As^{(V)}$ before being incorporated into calcite and the resulting calcite contained 36% $As^{(III)}$ and 64% $As^{(V)}$. All these experimental results confirm that $As^{(V)}$ has a much stronger interaction with calcite than $As^{(III)}$ and that calcite may represent an important reservoir for arsenic in various geological environments.

1. INTRODUCTION

Calcium carbonate, a major constituent of the rocks in the Earth's upper crust, has the ability to trap several kinds of ions in its structure. Among them, cations (Paquette and Reeder, 1995; Rimstidt et al., 1998; Davis et al., 2000; Stipp et al., 2006), and anions (Dove and Hochella, 1993; Alexandratos et al., 2007; Montes-Hernandez et al., 2009) could be incorporated or interact with mineral surfaces, making calcite a potential sink for these elements at the global scale. Several studies have characterized how arsenic, phosphorous or selenium oxyanions could be incorporated during the growth of calcite crystals at near surface conditions (Montes-Hernandez et al., 2009, 2011; Aurelio et al., 2010). Here, we report on time-lapse in situ observations

* Corresponding author at: Univ. Grenoble Alpes, ISTerre, BP 53, F-38041 Grenoble, France. Tel.: +33 476635907.
E-mail address: francois.renard@ujf-grenoble.fr (F. Renard).

http://dx.doi.org/10.1016/j.gca.2015.03.025
0016-7037/

of the interactions between arsenic oxyanions with calcite surfaces during growth, dissolution, and co-precipitation.

Arsenic exists in nature in four oxidation states. $As^{(-I)}$ in arsenian pyrite (Simon et al., 1999) and $As^{(-III)}$ (as arsenide) are mainly found in native minerals and metallic alloys containing arsenic, and $As^{(III)}$ (arsenite compounds) and $As^{(V)}$ (arsenate compounds) are present as constituents of various minerals and organic compounds or as oxyanions dissolved in groundwater (arsenite AsO_3^{3-} and arsenate AsO_4^{3-} anions, respectively) in which they can be transported. $As^{(III)}$ species are more soluble and toxic than $As^{(V)}$ species (Cullen and Reimer, 1989). $As^{(V)}$ is the dominant species under oxidized conditions, whereas $As^{(III)}$ is stable at intermediate to low redox potentials.

Arsenic has both toxic and carcinogenic effects on animals and humans and has accumulated to phytotoxic levels in some soils and groundwaters because of both human activity (e.g. use of pesticides in agriculture, mining activities, industry) and natural processes (e.g. rock– and mineral–fluid interaction such as during weathering). It represents a key environmental health problem in many countries (Christen, 2001; Rodrìguez-Lado et al., 2013), especially when it affects drinking water. The drinking guideline of 10 micrograms per liter (10 ppb) is recommended by the World Health Organization and used as the maximum contaminant level by the European Union and the USA. Hazard assessment associated with natural arsenic enrichment in soils and groundwaters depends heavily on the ability to understand and predict the mobility of arsenic and its transport between various reservoirs. In addition, there is growing interest in characterizing the effects of potential leakage of carbon dioxide repositories into freshwater aquifers, and the risk of toxic element release due to pH decrease and the dissolution of some minerals or the desorption of some species (Montes-Hernandez et al., 2013) during dissolution–precipitation processes (Putnis, 2009; Ruiz-Agudo et al., 2012).

Because of the importance of arsenic in various natural environments, we first describe in the following sections various hydrological systems with arsenic contaminations. Then, we report on various environmental systems where arsenic and calcite have been shown to interact. Finally, we present several mechanisms of arsenic–calcite interactions that have been proposed in the literature.

1.1. Arsenic in groundwaters and its origin

Various studies have pointed to contamination of groundwater by arsenic, well above the drinking guidelines and have demonstrated widespread dissolved arsenic concentrations in the range 0.05–3 ppm, and above 100 ppm in some localized contaminated sites. Usually arsenic has a geogenic origin, coming from the weathering of bedrock. In several mining areas, associated mine and drainage waters are contaminated. Mine tailings are leached by rain and arsenic has been transported to nearby groundwater reservoirs contaminating the soils in agricultural fields, leading to serious health problems (Carillo and Drever, 1998; Romero et al., 2004).

Up to 0.05 ppm was measured in the freshwaters in eastern New England, USA with more than 200,000 people using this water (Ayotte et al., 2003), up to 3 ppm in Vietnam (Christen, 2001), up to 1.3 ppm in Bangladesh (Zheng et al., 2004), above 0.05 ppm in the San Antonio-El Triunfo mining area in southern Baja California peninsula, Mexico (Carillo and Drever, 1998), and up to 0.65 ppm in the mining area of the Zimápan valley, Mexico (Romero et al. 2004; Song et al., 2006). In the calcareous environment of the Matehuala-Cerrito Blanco area, northern Mexico, Martínez-Villegas et al. (2013) reported concentrations in groundwaters as high as 158 ppm, with average values in the range 5–10 ppm. There, the dissolved arsenic is proposed to originate from the leaching of the abandoned wastes of mines. In an industrial area contaminated with by-products of arsenic ore exploitation, the mineral wastes were drained by meteoritic water and concentrations of dissolved arsenic as high as 235 ppm were measured (Julliot et al., 1999), in water with a pH down to 2.1. Bowell and Parshley (2005) have shown that the experimental leaching of rocks in a pit-lake could release up to 165 ppm dissolved arsenic.

In many environments, the distribution of arsenic concentrations in the water table of a given area is heterogeneous, with patches of high concentrations (Charlet et al., 2007). Arsenic concentrations above 50 ppb, the permissible current drinking level in Bangladesh, are found in over 30% of the wells of this country (Zheng et al., 2004) and more than 19.6 million inhabitants in China are living in areas where a risk of geogenic arsenic contamination has been estimated (Rodrìguez-Lado et al., 2013). In the aquifers of the southwest Songnen basin, China, residents are exposed to drinking water with more than 0.34 ppm of total arsenic (60–80% $As^{(III)}$, 20–40% $As^{(V)}$), with deeper groundwater showing on average higher arsenic concentrations (Guo et al., 2014). The sediments hosting the aquifer there contain between 2 and 102 ppm arsenic, which is bound to carbonates, iron oxides and clays and some arsenic is incorporated into siderite and calcite (Guo et al., 2014). In the Ganges delta, the concentration of arsenic in groundwater is very heterogeneous. Arsenic is present in carbonates and iron-oxide rich sediments, with associated concentrations in groundwater up to 0.5 ppm. There, the proportion of $As^{(III)}$ and $As^{(V)}$ are 42% and 58%, respectively (Charlet et al., 2007). In these sediments, the total concentration of arsenic is close to 3 ppm and major carriers are the amorphous iron oxides, sulfides and/or carbonates that liberate arsenic when they dissolve. The leaching of arsenic in the Marshall sandstone (Michigan) into the groundwater was attributed to the reaction between dissolved bicarbonate and arsenic-rich sulphide minerals initially present in the rock (Kim et al., 2000). As a result, the groundwater contains concentrations of arsenic in the range 0.2–0.3 ppm, mostly in the form of $As^{(III)}$. In the groundwater of the Chalkidiki area, Northern Greece, the concentration of arsenic in groundwaters reaches 3.7 ppm, mainly in the form of $As^{(V)}$, and some travertines have precipitated with concentrations up to 913 ppm $As^{(V)}$ trapped into the carbonate (Winkel et al., 2013). In this natural system, where the concentration of iron oxides is low and geothermal degasing of CO_2 is active, carbonates represent the main sink for arsenic uptake.

1.2. Arsenic in calcite-bearing rocks and contamination by leaching

Arsenic is often associated with pyrite and other sulfide minerals and found with gold in ore deposits or in coal and lignite, as described below. Gold mines in Nevada, USA, display 700–1500 ppm arsenic and contain 4–9% calcite and 18–31% dolomite in the bulk rock (Wells and Mullens, 1973). There, the process of ore formation involves the dissolution of calcite, creating pore space where gold and arsenic phases were precipitated. In Permian coals from the Gunnedah Basin, New South Wales, Australia, concentrations of arsenic of 40 ppm are measured, with up to 5% calcite (Ward et al., 1999). In lignite deposits of the Ioannina basin, Greece, between 2 and 46 ppm arsenic concentrations are measured (Gentzis et al., 1997), with calcite concentration between 0% and 17%. Arsenic in the Jáchymov mine, Czech Republic, is present in association with calcium in various secondary minerals (Ondrus et al., 1997). In all these types of rocks, coals and lignite, arsenic is mainly related to sulfur and sulphide minerals, and could have also interacted with nearby carbonate minerals.

Anomalous arsenic enrichment in hydrothermal calcite was measured near the Main Divide Fault in New Zealand with 35 ppm average arsenic, compared to 6 ppm average in the host rock (Horton et al., 2001). There, arsenic is contained in calcite in veins and fault gouge and no arseno-pyrite minerals were found in the faults. In sedimentary rocks extracted from road and railway tunnel projects in Hokkaido, Japan, the process of leaching could produce aqueous fluids with concentrations of pollutants much larger than recommended by environmental standards (Tabelin et al., 2014). Sediments show concentrations of arsenic in the rock in the range 9–19 ppm. Batch reactor leaching experiments on these samples showed the liberation of arsenic is mostly due to the dissolution of minerals, among them carbonates, iron oxides, and sulfides. Depending on the pH of the leaching fluid, up to 0.35 ppm of arsenic, mostly $As^{(V)}$, was concentrated in the leachate. In other limestones extracted from several well cores in Oklahoma, USA, up to 3.6 ppm of arsenic is present in calcite (Wunsch et al., 2014), raising the possibility of contamination of groundwater by CO_2 injection into geological repositories and subsequent calcite dissolution. Batch experiments of leaching of such rocks by CO_2-rich fluids showed that a concentration of arsenic of 30 ppb can be reached in 40 days, a high concentration controlled both by the dissolution of calcite and by desorption from other minerals (Wunsch et al., 2014).

1.3. Arsenic in calcite minerals: adsorbed and/or incorporated

Calcite may account for arsenic immobilization in natural environments where iron and aluminum oxides are absent or have lost their adsorbing effectiveness. For example natural carbonate travertines from Italy contain up to 270 ppm arsenic (di Benedetto et al., 2006; Bardelli et al., 2011; Costagliola et al. 2013) and several spectroscopic methods were used to decipher if $As^{(III)}$ or $As^{(V)}$ was preferentially incorporated. Using electron spin echo spectroscopy on these samples, it was proposed that the arsenic oxyanion $As^{(III)}$ was incorporated into the calcite, replacing the carbonate group (di Benedetto et al., 2006). Using X-ray Absorption Near Edge Structure (XANES), Extended X-ray Absorption Fine Structure (EXAFS) spectroscopy measurements, and Density Functional Theory (DFT) simulations, these authors concluded that $As^{(III)}$ could be incorporated in the calcite constituting these travertines; and that the incorporation of $As^{(III)}$ should induce an elongation along the calcite *c*-axis. They did not detect incorporation of $As^{(V)}$ in these samples and proposed that it was adsorbed on the surface (Bardelli et al., 2011). In a second series of measurements using XANES spectroscopy, Costagliola et al. (2013) proposed a different interpretation as they could measure that $As^{(V)}$ was preferentially incorporated in the calcite lattice and that some $As^{(III)}$ was present as well, at a level below 20% of the total arsenic, close to the detection limit. This indicates that arsenic uptake by calcite takes place mostly in the $As^{(V)}$ form, but that $As^{(III)}$ could be incorporated as well. These studies on arsenic–calcite interactions were all realized on natural micro-crystals, whereas nano-sized calcites are also present in the environment, and might interact differently with arsenic oxyanions.

To summarize, calcite is an important host phase for arsenic in the environment. Given that arsenic may be either incorporated in the calcite crystal lattice or adsorbed at the mineral surface (Cheng et al., 1999; Román-Ross et al., 2006; Alexandratos et al., 2007; Sø et al., 2008; Yokoyama et al., 2009, 2012), as in the case of iron-oxyhydroxides, calcite may provide a long-term effective trap, since its dissolution usually takes place faster only under acidic conditions, but it is rather insensitive to superficial exchange and redox reactions. Moreover calcite dissolution in the presence of arsenic may induce the precipitation of a wide variety of calcium-arsenic phases (Pierrot, 1964; Ondrus et al., 1997; Nordstrom et al., 2014). All these features make calcite a suitable and probably underestimated mineral trap for arsenic. As a consequence, identifying whether arsenic is adsorbed or incorporated into calcite has an important impact on its release rate calculated in fluid–rock interaction models for freshwater aquifers (Baerup et al., 2012). Although there is some knowledge on the binding mechanisms of arsenite and arsenate with calcite, no time-lapse in situ study has been performed to characterize how exactly arsenic interacts with calcite during dissolution or precipitation, and no study has been conducted on nano-calcite. In the present study, we analyze such a situation, by imaging at the nanometer scale the interactions of $As^{(III)}$ and $As^{(V)}$ oxyanions with calcite surfaces under far-from-equilibrium conditions where calcite either dissolves or precipitates, and characterize the reaction products using Raman spectroscopy. In parallel, we studied the sorption and co-precipitation of $As^{(III)}$ and $As^{(V)}$ during the formation of nano-calcite, and determined the redox state and binding mechanism of arsenic in calcite by ex situ synchrotron X-ray adsorption spectroscopy (XAS). Our results confirm that $As^{(V)}$ has a much larger effect on calcite growth than $As^{(III)}$ and that both oxyanions can be incorporated into

the calcite lattice structure. Moreover, we also identify how several crystallographic faces of calcite interact with arsenic.

2. METHODOLOGY

2.1. Calcite crystals

A calcite crystal (Iceland spar, Vizcaya, Mexico) was obtained from the Natural History Museum in London. ICP-OES (inductively coupled plasma-optical emission spectroscopy) revealed the high purity of the crystal, with only trace amounts of Mn (31 ppb), Mg (2.8 ppb) and Sr (11.4 ppb) detected. Rhombohedral fragments (ca. $4 \times 2 \times 1$ mm) were cleaved directly before each experiment from this single calcite crystal, parallel to the (10–14) cleavage plane.

2.2. Solutions for calcite dissolution under the AFM

Arsenic-free solutions and solutions with a controlled amount of arsenic ($As^{(III)}$ or $As^{(V)}$) were used for calcite dissolution experiments (Table 1). Several solutions with identical compositions were used to test the reproducibility of the obtained results. Firstly, arsenic-free aqueous solutions with controlled pH, between 7 and 11, and ionic strength equal to 0.016 or 0.047 M were injected into a flow-through fluid cell of an atomic force microscope (AFM) to dissolve the calcite surface. These solutions were prepared using doubled deionized water (resistivity > 18 mΩ cm) directly before each experiment. Sodium chloride and sodium hydroxide were used to adjust ionic strength and pH, respectively. The pH and salinity were adjusted according to thermodynamic simulations of equilibrated solutions using the PHREEQC software (Parkhurst and Appelo, 1999). Then, solutions with $As^{(III)}$ or $As^{(V)}$ oxyanions at concentrations of 5, 50, or 500 ppm, with the same ionic strength as the arsenic-free aqueous solutions initially used, were injected into the fluid cell, under several pH conditions (Table 1). The arsenic solutions were prepared from salts of sodium arsenite ($NaAsO_2$) and sodium arsenate dibasic heptahydrate ($Na_2HAsO_4{\cdot}7H_2O$) dissolved into double deionized water. The pH of the solutions was either controlled to be similar in the presence and in the absence of arsenic (experiments As-d-05 to As-d-09 in Table 1) or the pH was allowed to vary when arsenic was added (experiments As-d-01 to As-d-04 in Table 1). As well, the pH of all solutions was measured independently using a pH-meter confirming the PHREEQC simulation results. All chemical agents were obtained from Sigma Aldrich.

2.3. Solutions for calcite growth under the AFM

Solutions supersaturated with respect to calcite (Table 2) were prepared from $CaCl_2$ and $NaHCO_3$ 1 M stock solutions, following a procedure previously reported (Ruiz-Agudo and Putnis, 2012; Putnis et al., 2013). Stock solutions were produced at room temperature (23 ± 1 °C) from reagent grade sodium bicarbonate and calcium chloride salts that were dissolved into double-deionized water. The calcite growth solution was obtained by adding measured proportions of these two stock solutions to double-deionized water. The pH of the solutions was close to 8.8 and the Ca^{2+}/CO_3^{2-} ratio was equal to 1. The supersaturation of the solutions, Ω, was set to 6.46. Ω is defined here as $\Omega = IAP/K_{sp}$ where IAP is the ion activity product and K_{sp} is the calcite solubility product, equal to $10^{-8.48}$ at 25 °C, based on the PHREEQC database. Similarly, growth solutions containing various concentrations of arsenic $As^{(III)}$ or $As^{(V)}$ (5, 50, and 500 ppm) were prepared using the same arsenic-bearing salts as for the dissolution solutions. The proportions of the various solutions (stock solutions and arsenic solutions) were calculated using the PHREEQC software (Parkhurst and Appelo, 1999) to obtain solutions with the desired pH and salinity. Then the pH of the solutions was measured and adjusted to the desired value by adding small amounts of hydrochloric acid and sodium hydroxide, which did not modify significantly the ionic strength of the solutions.

2.4. Atomic force microscopy imaging

The calcite surfaces were scanned at room temperature (23 ± 1 °C) using a Bruker Multimode Atomic Force Microscope (AFM) operating in contact mode. The experiments were performed in situ within an O-ring sealed flow-through fluid cell from Digital Instruments (Bruker). The solutions were injected with a syringe between each scan, at regular time intervals of approximately 1.5 min, giving an effective flow rate of 22 $\mu L\ s^{-1}$. This flow rate ensures that processes occurring at the mineral surface are reaction-controlled, rather than diffusion controlled (Ruiz-Agudo et al., 2010a). AFM images were collected using Si_3N_4 tips (Veeco Instruments, tip model NP-S20) with spring constants 0.12 N m^{-1} and 0.58 N m^{-1}. Images were analyzed using the NanoScope software (Version 5.31r1). At the beginning of each growth or dissolution experiment, deionized water was injected over the calcite surface for several minutes, to observe dissolution and flatten the surface. Formation of etch pits (Fig. 1) can be observed during this step. Measurements of step retreat velocity (or etch pit spreading rate) and hillock (or spiral) step growth were made from sequential images scanned in the same direction. The retreat velocity during dissolution v_{sum} (nm s^{-1}) given by $v_{sum} = (v_+ + v_-)/2$ (where v_+ and v_- are the retreat velocities of + and − etch pit steps, respectively) was calculated measuring the length increase per unit time between opposite parallel steps in sequential images. The step spreading velocity was calculated in a similar way in the experiments in which 2D-nucleation was found as the main growth mechanism. When spiral growth was dominant, absolute growth velocities of obtuse (v_+) and acute (v_-) steps could be determined from measurements of geometric relationships of the spirals as in Larsen et al. (2010), Ruiz-Agudo et al. (2011), and Ruiz-Agudo and Putnis, 2012).

2.5. Raman spectroscopy

A confocal Raman spectrometer (Horiba Jobin Yvon XploRA) operating with the 638 nm line of a He–Ne laser

Table 1
List of AFM experiments of calcite dissolution in the presence of arsenic. A star * indicates solutions for which the pH was buffered in the presence of arsenic. For the other solutions, the pH increased due to increasing concentration of arsenic.

Exp. #	Ionic strength (mole/l)	Arsenic concentration	pH measured	Step velocity (nm/s)	Notes
As-d-01	0.016	0	6.2	1.9 ± 0.3	
		$As^{(V)}$, 5 ppm	7.5	3.2 ± 0.1	
		$As^{(V)}$, 50 ppm	10	2.5 ± 0.9	
		$As^{(V)}$, 500 ppm	11.1	1.9 ± 0.1	Presence of precipitates
As-d-02	0.016	0	6.1	3.7 ± 0.8	
		$As^{(V)}$, 5 ppm	8.9	3.3 ± 0.4	
		$As^{(V)}$, 50 ppm	10.4	2.3 ± 0.4	
		$As^{(V)}$, 500 ppm	11.2	2.5 ± 0.4	Presence of precipitates
As-d-03	0.047	0	6.1	4.5 ± 0.1	
		$As^{(V)}$, 5 ppm	8.9	3.6 ± 0.5	
		$As^{(V)}$, 50 ppm	10.4	1.8 ± 0.4	
		$As^{(V)}$, 500 ppm	11.2	1.5 ± 0.2	Presence of precipitates
As-d-04	0.047	0	6.1	2.0 ± 0.4	
		$As^{(III)}$, 5 ppm	8.8	1.9 ± 0.5	
		$As^{(III)}$, 50 ppm	9.5	1.2 ± 0.5	Rounded etch pits
		$As^{(III)}$, 500 ppm	9.2	1.3 ± 0.3	No precipitate
As-d-05*	0.047	0	5.6	4.5 ± 0.6	
		$As^{(V)}$, 5 ppm	6.9	4.1 ± 1.3	
		$As^{(V)}$, 50 ppm	7.6	4.4 ± 0.7	Rounded etch pits
		$As^{(V)}$, 500 ppm	8.1	4.9 ± 0.5	No precipitate
As-d-06*	0.047	0	5.4	1.9 ± 0.6	
		$As^{(V)}$, 5 ppm	5.2	3.0 ± 0.7	
		$As^{(V)}$, 50 ppm	5.5	5.9 ± 0.7	Slight distortion of etch pits
		$As^{(V)}$, 500 ppm	5.8	6.6 ± 0.8	No precipitate
As-d-07*	0.047	0	5.4	5.1 ± 0.9	
		$As^{(III)}$, 5 ppm	5.8	6.2 ± 0.6	
		$As^{(III)}$, 50 ppm	6.3	5.4 ± 0.7	
		$As^{(III)}$, 500 ppm	5.8	10.0 ± 0.9	No precipitate
As-d-08*	0.047	0	7.0	2.0 ± 0.5	
		0	11.0	1.8 ± 0.5	
		$As^{(III)}$, 50 ppm	11.0	1.1 ± 0.2	Rounded etch pits
		$As^{(III)}$, 500 ppm	11.0	1.1 ± 0.4	Presence of precipitates
As-d-09*	0.047	0	7.0	1.0 ± 0.2	
		0	11.0	1.5 ± 0.6	
		$As^{(V)}$, 50 ppm	11.0	1.8 ± 0.4	Slight distortion of etch pits
		$As^{(V)}$, 500 ppm	11.0	2.6 ± 0.4	No precipitate

was used for analysis of calcite surfaces after contact with $As^{(V)}$-bearing solutions. Two samples (As-d-02 and As-d-03, see Table 1), where dissolution of calcite occurred in the presence of 500 ppm of $As^{(V)}$ and precipitates formed, were selected for Raman investigations. Analyses were performed on flat areas and along step edges to search for Raman bands that are characteristic for arsenate vibrations. The heptahydrate sodium arsenate salt was also analyzed for reference. Each spectrum was taken with a 500 μm hole, 100 μm slit and 1800 grooves per millimeter grating using an acquisition time of 20 s. The signal-to-noise ratio was improved by averaging the results of ten consecutive measurements. Corrections for system drift were made using the 520.7 cm^{-1} Raman band of a silicon standard, measured at the beginning and the end of each Raman session, and the background was removed using the CrystalSleuth software.

2.6. Ex situ coprecipitation experiments using nanocalcite

Co-precipitation batch reactor experiments were performed to determine by ex situ X-ray absorption spectroscopy (XAS) if arsenate (four samples with various arsenate concentrations) and arsenite (one sample) are incorporated into a nanosized calcite structure (Table 3), and if their oxidation state is modified. In particular, we wanted to clarify whether arsenite is partly or totally oxidized into arsenate before being incorporated. For this purpose, calcite was synthesized by direct aqueous carbonation of portlandite at room temperature (23 °C) under anisobaric conditions ($Ca(OH)_2 + CO_2 \rightarrow CaCO_3 + H_2O$) (Montes-Hernandez et al., 2007). This method was chosen rather than homogeneous system (*e.g.* $Ca^{2+} + CO^{2-} \rightarrow CaCO_3$) because only calcite nanoparticles are produced after about two hours of reaction, leading to high-purity

Table 2
List of AFM experiments of calcite growth in the presence of arsenic. Step velocity (hillock or island) are given when three data or more could be measured.

Exp. #	Ionic strength (mole/l)	Arsenic concentration	pH measured	step velocity (nm.s^{-1})	Notes
As01	0.047	0	8.8	8.4 ± 1.6	Normal hillock
		$As^{(V)}$, 5 ppm	8.8	–	Normal hillock
		$As^{(V)}$, 50 ppm	8.8	7.7 ± 1.2	Rounded hillock
		$As^{(V)}$, 500 ppm	8.8	16.7	Tear-shaped hillock
As02	0.047	0	8.8	–	Normal hillock
		$As^{(V)}$, 500 ppm	8.8	–	Tear-shaped hillock
As03	0.047	0	8.8	–	Normal hillock
		$As^{(III)}$, 50 ppm	8.8	–	Normal hillock
		$As^{(III)}$, 500 ppm	9.2	–	Rounded hillock
As05	0.047	0	8.7	22.8 ± 0.1	Normal island
		$As^{(V)}$, 500 ppm	8.6	30.3 ± 12.5	Rounded island
As06	0.047	0	8.7	8.0 ± 4.5	Normal hillock
		$As^{(V)}$, 500 ppm	8.6	8.0 ± 4.7	Tear-shaped hillock
As08	0.047	0	11.0	13.9 ± 0.5	Normal island
		$As^{(III)}$, 500 ppm	11.0	3.3 ± 1.1	Scalloped island
		0	11.0	8.3 ± 0.1	Normal island
		$As^{(V)}$, 500 ppm	11.0	2.6 ± 0.7	Scalloped island
As09	0.047	0	11.0	–	Normal hillock
		$As^{(III)}$, 500 ppm	11.0	–	Rounded hillock
		0	11.0	–	Normal hillock
		$As^{(V)}$, 500 ppm	11.0	–	Rounded hillock

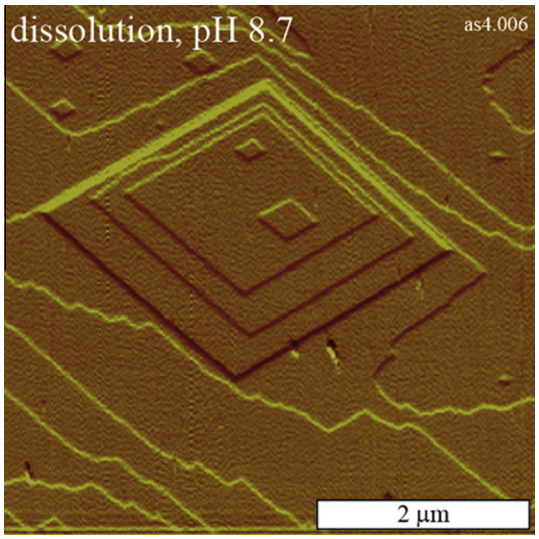

Fig. 1. In situ Atomic Force Microscopy (AFM) deflection image of a (10–14) calcite surface during dissolution in deionised, arsenic-free, water in a flow-through fluid cell. Dissolution occurs by spreading along 4-sided rhombohedral etch pits, with an obtuse angle of 102°. Calcite steps are mostly one unit cell (3.5 Å height).

homogeneous nanosized calcite crystals free of metastable carbonate phases such as amorphous calcium carbonate (ACC), vaterite or aragonite. The experimental protocol for the synthesis of nanocalcite in the presence of various oxyanions is described in Montes-Hernandez et al. (2009). The initial pH was 12.4, and then dropped to 5.5 once the portlandite was consumed and nanocalcite had formed. The solid phase was then isolated by centrifugation after 24 h. The initial concentration in the fluid and the final arsenic content in the solid calcite sample are given in Table 3.

2.7. X-ray absorption spectroscopy (XAS)

XAS measurements were carried out at the European Synchrotron Radiation Facility (ESRF, Grenoble, France), operating with a ring current of 100 mA. Arsenic *K*-edge EXAFS spectra were collected on the BM30B (FAME) beamline using a Si(220) double crystal monochromator with dynamic sagittal focusing. The photon flux was of the order of 10^{12} photons per second, and the spot size was 300 µm horizontal × 100 µm vertical (Proux et al., 2005). The spectra were collected in fluorescence mode with a 30-element solid-state germanium detector (Canberra). For the $As^{(V)}$-nanocalcite samples (four samples), four to six scans of 40 min each were acquired, and then averaged to reduce noise. The EXAFS spectra of arsenic salts used in the initial solutions were also taken as references for $As^{(III)}$ and $As^{(V)}$. Data from each detector channel were inspected for glitches or drop-outs before inclusion in the final average. Data analysis was performed using the IFEFFIT package (Ravel and Newville, 2005), including ATHENA for data extraction and ARTEMIS for the shell fitting. The value ranges for R and k were 0.7–4.0 Å and 2.8–13.7 Å^{-1}, respectively. Fitting was done in R-space using the Fourier transforms of the k^3-weighted $\chi(k)$ functions. Johnbaumite ($Ca_5(AsO_4)_3OH$)) structure was used to calculate FEFF phase and amplitude functions.

Table 3
Summary of batch-reactor nano-calcite precipitation experiments in presence of $As^{(V)}$ and $As^{(III)}$ and synchrotron XAS results.

Exp. #	Arsenic initial concentration in solution (mg As L^{-1})	Arsenic concentration in calcite from ICP-AES analyses (mg As kg^{-1} calcite)	XAS results
Calcite-$As^{(V)}$-1	18	500	Incorporated as $As^{(V)}$
Calcite-$As^{(V)}$-2	35	1000	Incorporated as $As^{(V)}$
Calcite-$As^{(V)}$-3	50	1400	Incorporated as $As^{(V)}$
Calcite-$As^{(V)}$-4	65	1990	Incorporated as $As^{(V)}$
Calcite-$As^{(III)}$-1	50	600	Incorporated as 64% $As^{(V)}$ and 36% $As^{(III)}$

For the $As^{(III)}$-nanocalcite sample, only the XANES part was recorded because of lack of beamtime, thus information on the local oxidation state only, and not on the local structure, was obtained. The spectrum was normalized and processed by linear combination fits (LCFs) with ATHENA to determine the proportion of $As^{(III)}$ and $As^{(V)}$.

3. RESULTS

3.1. In situ AFM calcite dissolution experiments

Direct in situ observations show that in contact with pure water, the (10–14) calcite surface starts dissolving along steps that retreat and through the formation of etch pits with typical rhombohedral shapes (Fig. 1), as already observed in previous studies (see Ruiz-Agudo et al., 2010b; Ruiz-Agudo and Putnis, 2012 and references therein). Etch pit steps are typically one unit cell (3.5Å) high.

Measured retreat rates (v_{sum}) in water ranged between 1.9 and 5.1 nm s^{-1}, with an average variability of ±0.5 nm s^{-1} within each experiment (Table 1), for solutions in the circumneutral pH range 5.4–6.1. These values agree well with previously published values of etch pit retreat rates for calcite in undersaturated solutions – see for example the review by Ruiz-Agudo and Putnis (2012) and references therein. Measured retreat rates values in arsenic-bearing solutions ranged from 1.5 up to 10 nm s^{-1}. For the solutions where the pH was not buffered in the presence of arsenic and was in the range 7.5–11.2 (experiments As-d-01 to As-d-04 in Table 1), the etch pit spreading rate was in the range 1.3–2.5 nm s^{-1}, and slightly decreased with increasing $As^{(III)}$ or $As^{(V)}$ concentration; nevertheless, this could be related to the increasing pH of the solutions and remains within the error bars of our measurements. However, for solutions with controlled pH in the range 5–6 (experiments As-d-05 to As-d-07 in Table 1), faster spreading rates were measured and increasing concentrations of $As^{(III)}$ or $As^{(V)}$ increases the etch pit retreat rate, up to 10 nm s^{-1} for the largest arsenic concentrations (500 ppm).

Arsenic has a clear effect on the shape of the etch pits, but only at high (500 ppm) concentrations. For example, in the presence of 50 ppm $As^{(V)}$ at pH 5, the shape of etch pits is not modified (Fig. 2a). However, at 500 ppm $As^{(V)}$ and the same pH, the angle of the etch pits increases from the normal value of 102–111° (Fig. 2b), indicating an interaction between the dissolved $As^{(V)}$ and the calcite surface. More interestingly, $As^{(III)}$ also has a strong effect on the morphology of the etch pits, at pH above 9 and 500 ppm concentration (Fig. 2c and e). The obtuse angle of the etch pit slightly increases to 105°, but the symmetric corner becomes rounded, indicated a pinning of the steps at this position. Nevertheless, this effect is not observed at circumneutral pH, even for the highest $As^{(III)}$ concentration.

Interestingly, together with dissolution, for the highest concentrations of $As^{(V)}$ (500 ppm), precipitates were observed forming on the calcite surface at pH 11 (Fig. 2d). Immediately on contact of the surface with the undersaturated solution, nucleation of tiny ~50 nm, initially scarce, particles precipitated on the calcite surface, more or less randomly, and without any observable preferred orientation. They covered a significant portion of the calcite surface within half an hour. The adhesion of these precipitates was initially weak as they were moved by the AFM tip.

Precipitated particles were generally too small to be easily identified by means of Raman spectroscopy. In flat areas with low particle density analyses showed no Raman bands other than those belonging to the calcite substrate. However, three weak and broad bands at 807, 851 and 881 cm^{-1} could be detected in areas close to deeper step edges where precipitates were typically present in higher concentration (Fig. 3a). These Raman band locations are characteristic for AsO_4 stretching modes of various crystalline arsenate phases, including Ca-arsenate phases such as pharmacolite ($CaHAsO_4{\cdot}2H_2O$) and johnbaumite ($Ca_5(AsO_4)_3OH$) as well as the sodium arsenate salt used in the experiments ($Na_2AsO_4{\cdot}7H_2O$) (Fig. 3b). The precipitate is thus interpreted to be an arsenate-bearing phase. Normally broader and less intense peaks are a sign for low crystallinity and this seems to be the case for this arsenate phase. However, a more precise identification and quantification is difficult because of the rather weak signal in our measurements and the lack of comprehensive literature data on all the possible arsenate phases.

3.2. In situ AFM calcite growth experiments

The presence of high concentrations of arsenic (50 ppm and above) affects the morphology and rate of calcite growth. The (10–14) cleavage surface of calcite commonly grows by the formation of spirals in which pyramidal hillocks, located above a screw dislocation defect, grow along

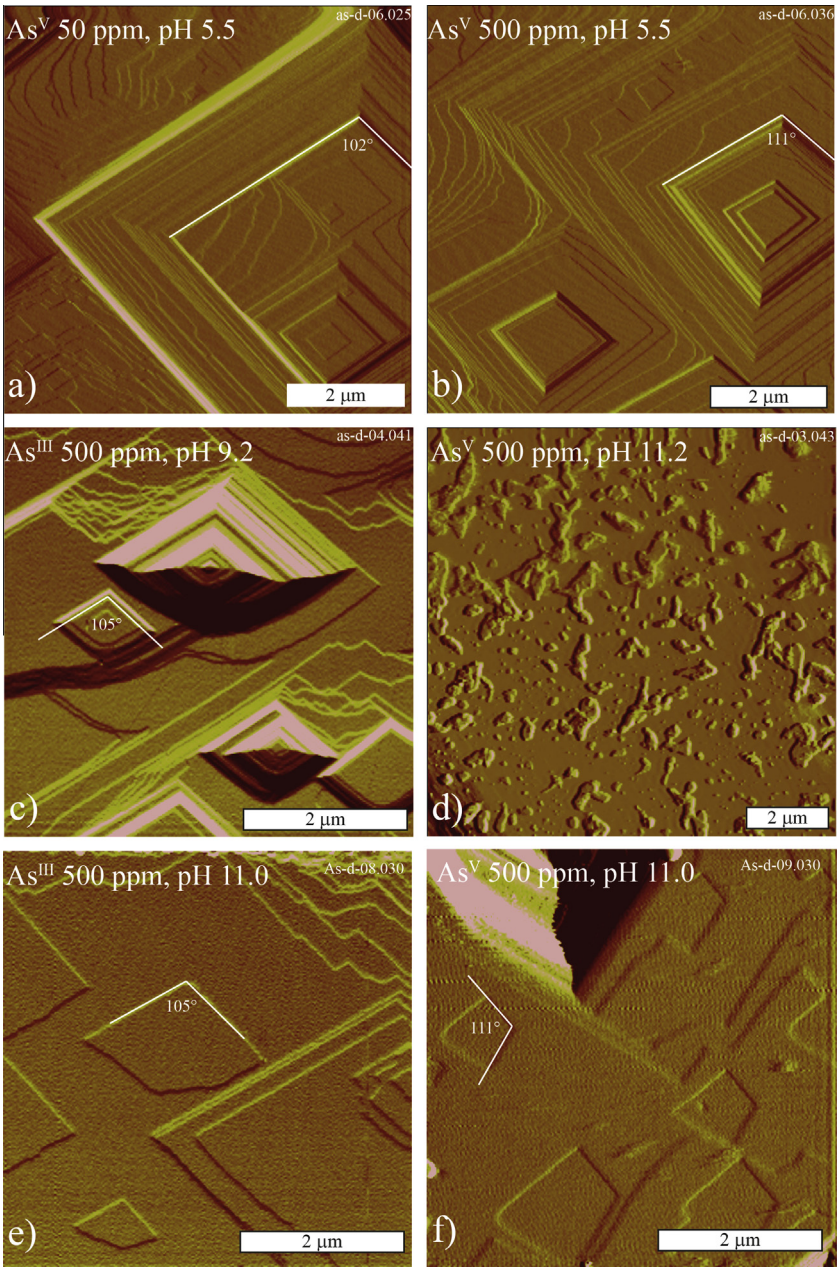

Fig. 2. In situ AFM deflection images of (10–14) calcite cleavage surfaces during dissolution in a flow-through fluid cell. (a) Dissolution in deionised, arsenic-free, water, showing typical rhombohedral etch pits with an angle of 102°. (b) Dissolution in the presence of As$^{(V)}$, 500 ppm, same pH as in (a), showing that the angle of the etch pit has increased to 111°, giving a distortion to the original rhombohedral form. (c) Dissolution in the presence of As$^{(III)}$, 500 ppm, showing a strong effect on the shape of the etch pit, with two sides that are pinned and dissolved much slower. (d) At high pH and with 500 ppm As$^{(V)}$, some precipitates form at the surface of calcite during its dissolution in deionised water. Precipitates mainly localize along macrosteps or in etch pits where dissolution is faster. (e) Dissolution in the presence of As$^{(III)}$, 500 ppm and pH 11, showing a strong effect on the shape of the etch pit where two sides are pinned. (f) Dissolution in the presence of As$^{(V)}$, 500 ppm and pH 11, showing a distortion of the original rhombohedral form.

four steps that form obtuse and acute angles of a rhombohedrum (Fig. 4a; see also Ruiz-Agudo and Putnis (2012)). In addition, calcite growth occurs by the nucleation and growth of rhombohedral islands (Figs. 5 and 6).

An effect of As$^{(III)}$ could be observed only for the highest concentration of 500 ppm at pH in the range 8–11. The initial regular spiral hillock (Fig. 4a) shows a rounding of the acute angle in the presence of arsenic. This change in morphology occurs within a minute after injection of an arsenic bearing solution (Fig. 4b). This effect could not be observed for the lower As$^{(III)}$ concentrations of 5 and 50 ppm. Conversely, As$^{(V)}$ shows clear effects not only at 500 ppm, but at 50 ppm as well (Fig. 4c and d, Figs. 5 and 7). As in the case of As$^{(III)}$, the acute step of the spiral hillocks

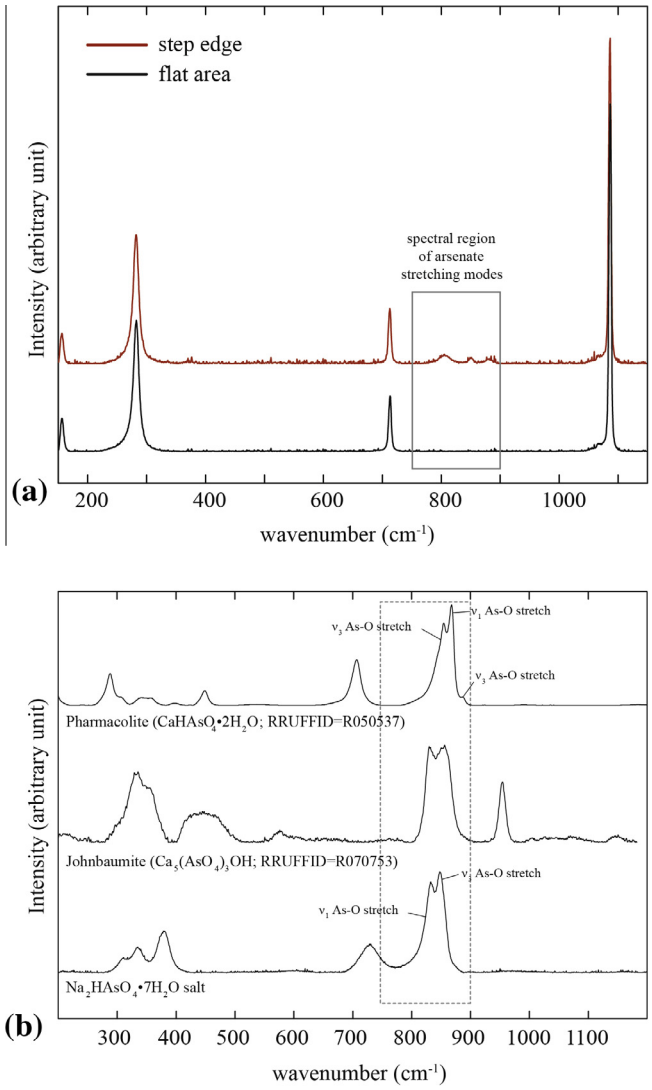

Fig. 3. (a) Raman spectra of the calcite surface used for experiment As-d-03. Raman spectra of flat areas (black) only reveal peaks of the calcite substrate, whereas the Raman spectrum taken close to a deeper step edge (red) reveals three additional weak and broad peaks in the 800–900 cm^{-1} region, characteristic for arsenate stretching vibrations. (b) Reference Raman spectra for pharmacolite, johnbaumite and heptahydrate sodium arsenate. Peak assignments for pharmacolite and heptahydrate sodium arsenate are according to Frost et al. (2010) and Vansant et al. (1973), respectively. (For interpretation of the references to colour in this figure legend, the reader is referred to the web version of this article.)

becomes rounded at 50 ppm, and upon further increase of the $As^{(V)}$ concentration the whole pyramidal morphology is altered into a tear-shape at 500 ppm by pinning of the acute angle. This transformation occurs within minutes (Fig. 7a and b). However, the original rhombohedral pyramidal shape recovers very fast (after a few scans) as soon as an arsenic-free growth solution is injected in the flow-through cell (Fig. 7d and e). In those experiments in which growth occurred mostly by 2D island nucleation and spreading, the shape of growth islands is modified, from rhombohedral (Fig. 5a) to rounded (Fig. 5b). At pH 11 and in the presence of 500 ppm of $As^{(III)}$ or $As^{(V)}$, the islands become scalloped and rounded (Figs. 6a and c), but recover their initial morphology within minutes when an arsenic-free fluid at the same pH is injected (Fig. 6b). The rate of island spreading is considerably slowed down (see Table 3) in the presence of $As^{(III)}$ at 500 ppm, and drops from a value close to 14 nm s^{-1} in water at pH 11 to less than 4 nm s^{-1} with arsenite.

3.3. Ex situ coprecipitation experiments using nanocalcite

The nanocalcite prepared in the presence of 50 ppm $As^{(V)}$ and $As^{(III)}$ contained 1.4 and 0.6 mg g^{-1} arsenic, respectively (Table 3). Thus, the arsenic partitioning in the solid phase is roughly doubled from $As^{(III)}$ to $As^{(V)}$. As a comparison, Yokoyama et al. (2012) observed a factor of about ten with the sorption-coprecipitation method at pH 12. Thus, the protocol used in their study to form nanocalcite enhances the fixation of $As^{(III)}$. The redox state

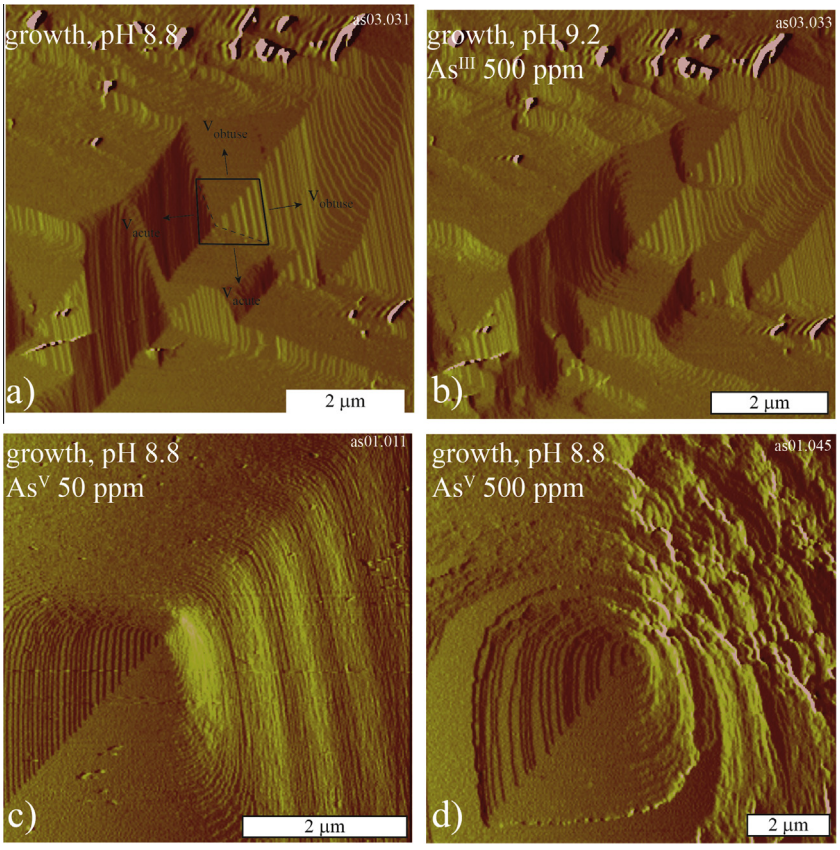

Fig. 4. AFM deflection images of the effect of arsenic during growth of calcite on the (10–14) cleavage surface. (a) Pyramidal hillock with acute and obtuse angles indicated and the corresponding step velocities v_{obtuse} and v_{acute}, respectively. (b) Effect of $As^{(III)}$, 500 ppm is characterized by a slight rounding of the acute angle. (c) Effect of $As^{(V)}$, 50 ppm, characterized by a slight rounding of the acute angle. (d) Strong effect of $As^{(V)}$, 500 ppm, with the transformation of the pyramidal hillock morphology into tear shape by pinning the acute angle.

and local structure of arsenic in $As^{(III)}$- and $As^{(V)}$-coprecipitated nanocalcites concentration were studied by arsenic K-edge XANES and EXAFS spectroscopy. For $As^{(V)}$, four concentrations were tested. The four samples showed identical XANES and EXAFS spectra (Supplementary Material, Fig. S1). The position of the absorption edge was consistent with pentavalent arsenic, so no change in arsenic redox state was observed. The four EXAFS spectra (Fig. S1b) were averaged for EXAFS analysis, to increase the signal to noise ratio (Fig. 8a), and is referred to as $As^{(V)}$-nanocalcite hereafter. The averaged spectrum was intermediate between adsorbed and $As^{(V)}$-calcite previously studied by Alexandratos et al. (2007) (Fig. 8a). On the Fourier transformed spectrum, the peak corresponding to Ca shells (at $R + \Delta R = 2.5$–3.5 Å) had a shape slightly different from these two reference compounds, with shoulders at 4.5 and 6 $Å^{-1}$ less marked than in $As^{(V)}$-coprecipitated calcite (arrows in Fig. 8b). We verified that our shell fitting of the adsorbed and coprecipitated $As^{(V)}$-calcite spectra provided by Alexandratos et al. (2007) provided the same structural parameters as those published, within error (±0.02 Å for the interatomic distance R and ±0.5 for the coordination number CN), see Table S2 in the Supplementary Material. In the $As^{(V)}$-nanocalcite, arsenic is surrounded by 2.9 Ca atoms at 3.49 Å and 2.20 Ca atoms at 3.67 Å. These values are similar to those obtained by Alexandratos et al. (2007) and by Yokoyama et al. (2012) for $As^{(V)}$-coprecipitated calcite, with small differences (±0.08 Å for R and ±1 for CN) between the three samples. This comparison suggests that the AsO_4 tetrahedron is incorporated in the calcite structure and accommodated in a similar way in micro- and nano-sized calcite crystals.

The XANES spectrum for arsenic in $As^{(III)}$-coprecipitated nanocalcite is intermediate between that of $As^{(V)}$ and $As^{(III)}$ salt references. It is correctly fitted by a combination of 64% of the former and 36% of the latter (Fig. 8c). Thus, 64% of $As^{(III)}$ was oxidized into $As^{(V)}$ before or after incorporation in calcite, whereas 36% was incorporated as $As^{(III)}$. These observations are partly consistent with those by Yokoyama et al. (2012). These authors showed that at pH above 9, $As^{(III)}$ was partly auto-oxidized into $As^{(V)}$ in the solution before being incorporated in calcite, and partly incorporated as $As^{(III)}$, and that this latter species was then oxidized into $As^{(V)}$ within 24 h. In the present study, a significant proportion of arsenic remained as $As^{(III)}$ in the structure.

To summarize, incorporation of $As^{(V)}$ in nanocalcite is higher than $As^{(III)}$, but only by a factor of two, as compared to 10 for calcite at pH 12. $As^{(V)}$ was incorporated in the calcite crystal lattice as a CO_3^{2-} substitute in a similar way as

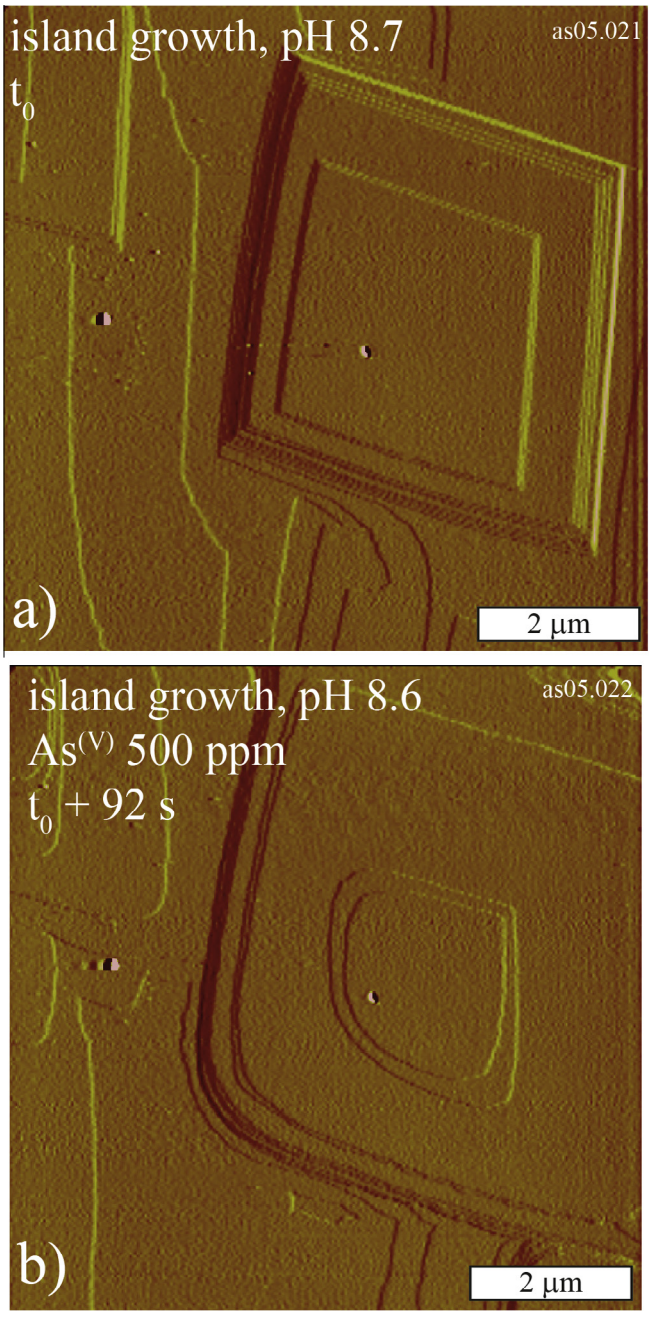

Fig. 5. AFM images of the growth of calcite islands. The time of arsenic injection is indicated as t_0. (a) Island during calcite growth in the absence of arsenic. (b) Island during calcite growth in the presence of 500 ppm arsenic and showing the rounding of one obtuse corner of the island.

previously observed (Alexandratos et al., 2007; Yokoyama et al., 2012). $As^{(III)}$ was partly oxidized into $As^{(V)}$, but 36% of arsenic present in calcite remained in the $As^{(III)}$ state.

4. DISCUSSION

4.1. Interaction of $As^{(III)}$ and $As^{(V)}$ with calcite surfaces

Experimental and natural studies existing in the literature on the interaction of arsenic with calcite often show contradictory results. While some studies have proposed that $As^{(III)}$ can be adsorbed or incorporated into calcite (Cheng et al., 1999; Román-Ross et al., 2006; Bardelli et al., 2011), other studies suggested that most of the incorporated arsenic, if not all, is $As^{(V)}$ and that $As^{(III)}$ interacts weakly with calcite (Sø et al., 2008; Yokoyama et al., 2009, 2012; Costagliola et al., 2013).

In a study performed using X-ray standing waves, it was proposed that $As^{(III)}$ was adsorbed on the calcite surface and located at the carbonate site (Cheng et al., 1999), the

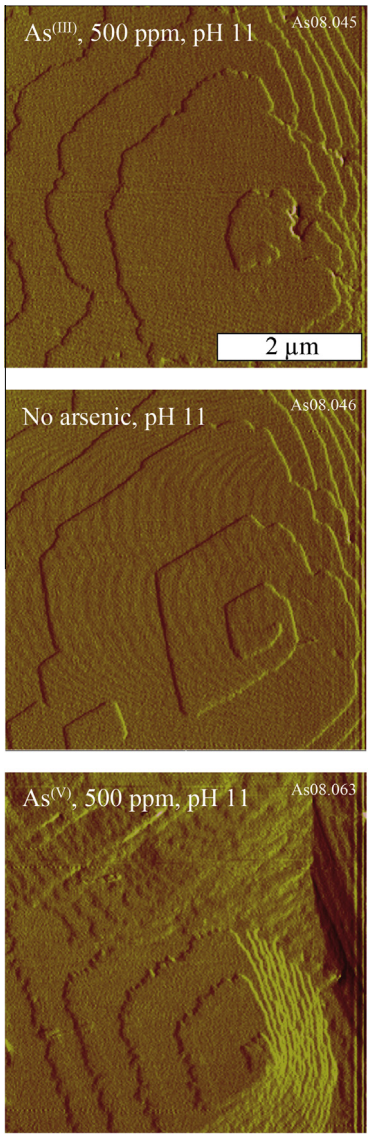

Fig. 6. AFM images of the growth of calcite along one island at pH 11. (a) Island during calcite growth in the presence of 500 ppm of $As^{(III)}$ and showing the scalloping of the steps and rounding of the island. (b) Island during calcite growth in the absence of arsenic. (c) Island during calcite growth in the presence of 500 ppm of $As^{(V)}$ and showing the scalloping and rounding of the island. These three images were acquired during the same experiment (As08, see Table 2), and the morphology changed within 1.5 min upon injection of a fluid with a new composition.

oxygen base of the arsenite oxyanion was coincident with the plane of the carbonate group while the arsenic atom was pointing away from the calcite (10–14) surface. In a set of experiments of the interaction of calcite and $As^{(III)}$ at pH 7.5, Román-Ross et al. (2006) showed that calcium arsenite could precipitate as a solid solution with calcite, inducing a volume change in calcite supercells that is proportional to the initial arsenic concentration in the fluid and that an average of $2250 \pm 20\%$ ppm of $As^{(III)}$ could be incorporated into the calcite structure, with a transition from adsorption to coprecipitation with increasing arsenite concentration.

Alexandratos et al. (2007) showed that $As^{(V)}$ interacted with calcite both by sorption and co-precipitation, with preferential incorporation of $As^{(V)}$ at the (10–14) calcite surface. In their experiments, $As^{(V)}$ was incorporated preferentially along the obtuse angle (– steps) of growth hillocks and induced the formation of macrosteps, as observed in our experiments. Moreover, based on EXAFS measurements and modeling, they proposed that $As^{(V)}$ oxyanions were replacing the carbonate group in the calcite crystal. In a series of batch sorption experiments at pH 6–9.1 and low arsenic concentrations (2.5 ppm), Sø et al. (2008) showed that $As^{(V)}$ was adsorbed onto calcite and modelled the sorption using $H_2AsO_4^-$ and $CaHAsO_4^0$ as adsorbing species. These authors showed that $As^{(III)}$ was not adsorbed on calcite at these low concentrations. Using batch reactor experiments, as well as XANES and EXAFS spectroscopy, Yokoyama et al. (2009) measured that $As^{(III)}$ did not coprecipitate with calcite, whereas $As^{(V)}$ did and replaced the carbonate group in the calcite structure in a pH range between 7 and 12.

In a more recent study, Yokoyama et al. (2012) performed sorption and coprecipitation experiments with low arsenic concentration in the fluid (around 0.4–6 ppm), and adsorption experiments with 750 ppm arsenic in the fluid. At pH above 9, they observed a direct incorporation of $As^{(III)}$ in early precipitated calcite and vaterite crystals, as observed in EXAFS spectra. Up to 33% of arsenic was in the $As^{(III)}$ oxidation state when incorporated at pH 11. However, this species was transient since the final calcite contained only $As^{(V)}$ (Yokoyama et al., 2012).

In the present study, we observe directly that $As^{(V)}$ has a stronger interaction than $As^{(III)}$ with calcite during its growth at room temperature, changing the characteristic pyramidal growth hillock morphology into a tear-shaped form, as already observed for selenium oxyanion incorporation into calcite (Renard et al., 2013). This effect is quickly reversed upon injection of an arsenic-free growth solution. On the contrary, only at pH 11 and the highest 500 ppm concentration does $As^{(III)}$ show some interaction with calcite (pinning of etch pits during dissolution and roughening of the surface and slowing down of island growth rate during growth). Additional ex situ measurements by XAS spectroscopy confirms that $As^{(V)}$ is preferentially incorporated into calcite (~2 times higher) with respect to $As^{(III)}$. $As^{(V)}$ is preferentially incorporated into calcite because $HAsO_4^{-2}$ dominant ions can easily substitute the carbonate ions during calcite formation at any given conditions. In addition, Yokoyama et al. (2012) suggested that the formation of $CaHAsO_4^-$ complexes in solution might facilitate the incorporation of $As^{(V)}$ in calcite. We did observe the incorporation of $As^{(III)}$ in our experimental conditions (pH > 11) both in AFM and in batch-reactor, which is consistent with the presence of negatively charged species $HAsO_3^{-2}$, dominant at pH > 9. In addition, during calcite formation in the batch reactor experiments, $As^{(III)}$ was significantly oxidized to $As^{(V)}$. This oxidation may be catalyzed by the surface, but further research would be needed to confirm it. The resulting nanocalcite contained 64% $As^{(V)}$ and 34% $As^{(III)}$. These results are consistent with previous results obtained by Yokoyama et al. (2012) who

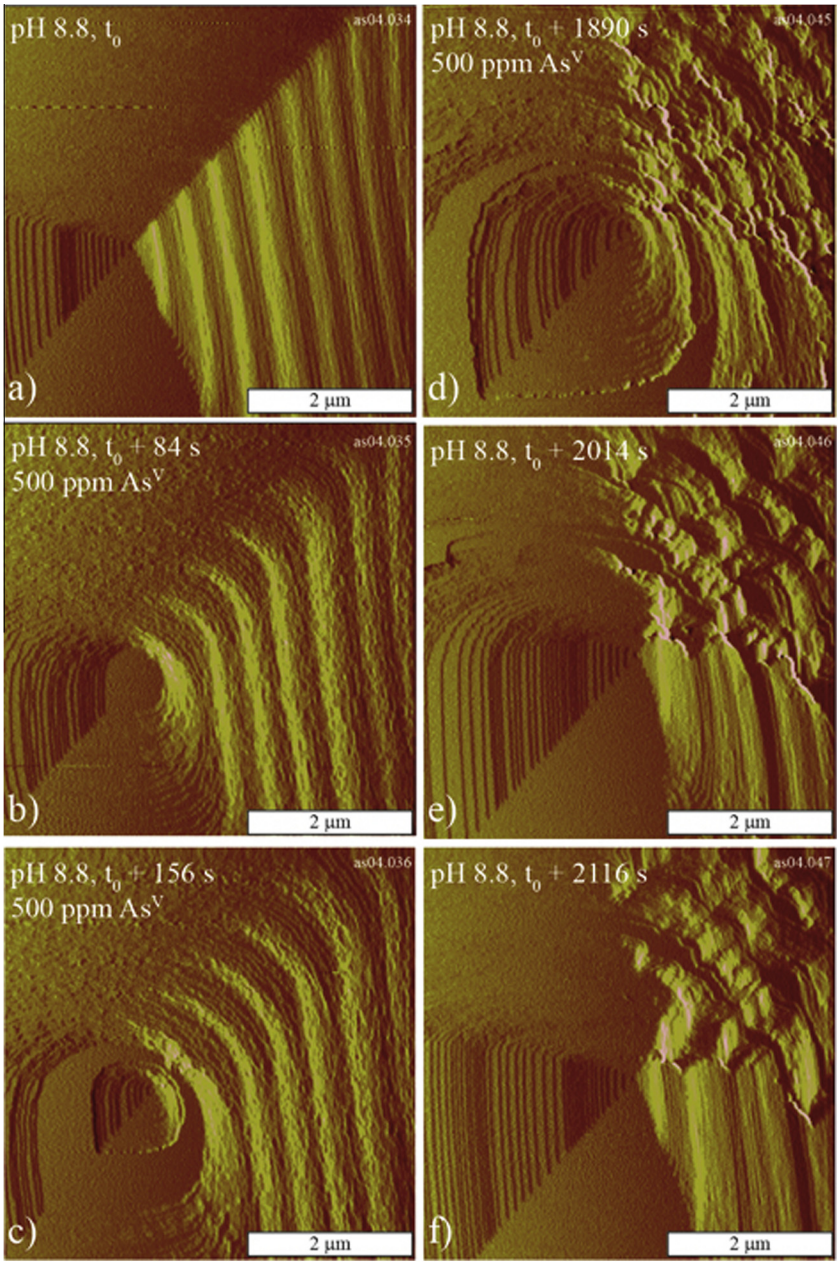

Fig. 7. Time-lapse in situ AFM images of a (10–14) calcite surface during growth in the presence of $As^{(V)}$ in a flow-through fluid cell. The time of the first arsenic injection is indicated as t_0. (a) Typical pyramidal hillock when no arsenic is present. (b–d) With the addition of 500 ppm $As^{(V)}$, the hillock is strongly deformed, with pinning of one acute angle. (e–f) When the same arsenic-free solution as in (a) is re-injected at time t_0 +1900 s, the hillock recovers its initial shape within 100 s.

used a different calcite coprecipitation protocol. Thus, incorporation mechanisms of $As^{(V)}$ and $As^{(III)}$ seems to be similar in calcite and nanocalcite. Small differences may be highlighted, though. Yokoyama et al. (2012) suggested a preferential trapping of $As^{(III)}$ within vaterite (precursor of calcite), whereas in our study $As^{(III)}$ was identified in nanocalcite containing 100% calcite, and no vaterite could be detected in the batch reactor products. Note that the experimental protocols were different: Yokoyama et al. (2012) produced vaterite as a precursor which was a better sink for $As^{(III)}$, whereas in our coprecipitation experiments no vaterite was produced (Montes-Hernandez et al., 2009). Moreover, after 24 h $As^{(III)}$ was completely converted into $As^{(V)}$ for their experiments whereas in our case, 34% of incorporated arsenic remained as $As^{(III)}$.

AFM measurements reveal that high concentrations (500 ppm) of $As^{(III)}$ also produce growth modifications (Figs. 4–6). Concerning the dissolution of calcite in the presence of arsenic, both $As^{(V)}$ and $As^{(III)}$ species have a small effect on the shape of the etch pits, with etch pits showing rounding of one of the obtuse corners only at the highest $As^{(III)}$ concentration tested (500 ppm). As well,

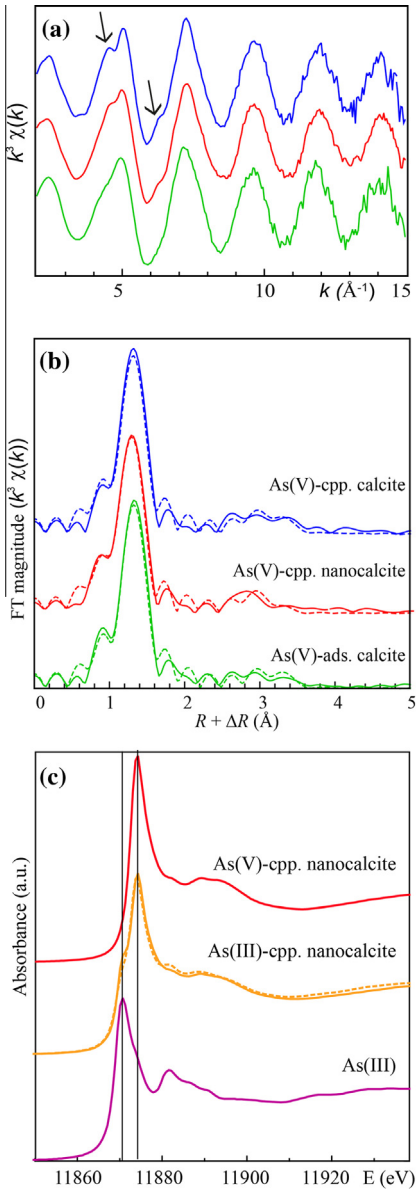

Fig. 8. (a) Arsenic K-edge EXAFS spectrum for the $As^{(V)}$-coprecipitated nanocalcite (red) compared with 100 μM $As^{(V)}$–calcite sorption sample (green) and $As^{(V)}$–calcite single crystal coprecipitation samples (blue) previously published by Alexandratos et al. (2007). The $As^{(V)}$-coprecipitated nanocalcite is the average of identical spectra presented in Fig. S1. Arrows point to well-marked shoulders on the $As^{(V)}$-coprecipitated calcite spectrum, and less pronounced on the $As^{(V)}$-coprecipitated nanocalcite. b) Corresponding Fourier transforms (not corrected for phase shifts) and shell fittings (dashed lines) using the same color code. (c) Arsenic K-edge XANES spectra for the for the $As^{(V)}$- and $As^{(III)}$-coprecipitated nanocalcites (pink and yellow, respectively) and for As_2O_3 ($As^{(III)}$, purple). Each spectrum is an average of 4–6 XANES acquisitions. The $As^{(III)}$-coprecipitated nanocalcite spectrum was fitted with a combination of 36% $As^{(III)}$ +64% $As^{(V)}$-coprecipitated nanocalcite (R factor = 0.0018, dashed line). (For interpretation of the references to colour in this figure legend, the reader is referred to the web version of this article.)

arsenic oxyanions induce a slight increase in the dissolution rate (see Table 1). According to these observations and taken into account that the EXAFS measurements suggest that $As^{(V)}$ is partially adsorbed and coprecipitated, we propose that the adsorption/incorporation of $As^{(V)}$ is responsible for the observed modifications in growth and adsorption/co-precipitation in dissolution features. Conversely, $As^{(III)}$ can also be slightly adsorbed and/or incorporated, but it has a weaker effect than $As^{(V)}$.

Detailed AFM observations of the morphology changes induced in growth and dissolution features by the presence of $As^{(V)}$ shows that the changes can be related to the development of etch pits with step edges parallel to [42−1] or [010]. These directions correspond to the intersection of the {0112} and {0001} form with the cleavage rhombohedrum, as indicated by morphology simulations performed using SHAPE software assuming overdevelopment of those faces (Fig. 9). The (0112) and (0001) faces are polar and consist of alternate layers of Ca^{2+} and CO_3^{2-} ions in successive planes. Thus, they are not stable under normal growth conditions. The adsorption of charged arsenic species may stabilize the hydration water molecules on these faces and thus reduce repulsive interactions between positive (or negative) like-charges. Thus we hypothesize that the presence of arsenic species, and particularly $As^{(V)}$, may neutralize the dipole moment of polar faces, resulting in stabilization of the (0112) or (0001) faces. This is reflected in changes in the morphology of calcite growth and dissolution features, in particular in the observation of edges parallel to (010) and (42−1) directions. The opposite situation, *i.e.* reduced attractive interactions between unlike charges and destabilization of stable faces, also takes place. The fact that surface morphology changes are reversible upon injection of arsenic-free solutions and that similar changes are observed during dissolution, where ion incorporation is less likely, suggests that the $As^{(V)}$ ions causing such a morphology change are adsorbed. Note that similar ideas have been used to explain the effect of both inorganic (Li^+, Wang et al., 2011) and organic (HEDP, Ruiz-Agudo et al., 2010b) impurities on calcite growth. Nevertheless, this does not exclude the possibility that a fraction of the arsenic is actually incorporated into the growing calcite, a fact that cannot be exclusively confirmed by AFM observations and that was observed by Cheng et al. (1999), who described a very specific mechanism of adsorption, i.e. surface incorporation. At pH close to 9, $As^{(III)}$ oxyanions are present in the solution in two forms that have a charge equal to either 0 (H_3AsO_3) or −1 ($H_2AsO_3^-$) (see Fig. S3); thus, in the framework of the above-explained model it is easy to understand that $As^{(III)}$ shows a weaker interaction than $As^{(V)}$ (which is present exclusively in the form of $HAsO_4^{2-}$, i.e. a doubly charged anion) with the calcite surfaces during growth. Several arsenite species were not present in this database so their stability constants were taken from the literature (Table 4).

Several AFM growth experiments were performed at constant pH of 8.8, and at this pH the main $As^{(V)}$ species (97%) is doubly charged ($HAsO_4^{2-}$), while the main $As^{(III)}$ species (70%) is uncharged (H_3AsO_3), so that it cannot

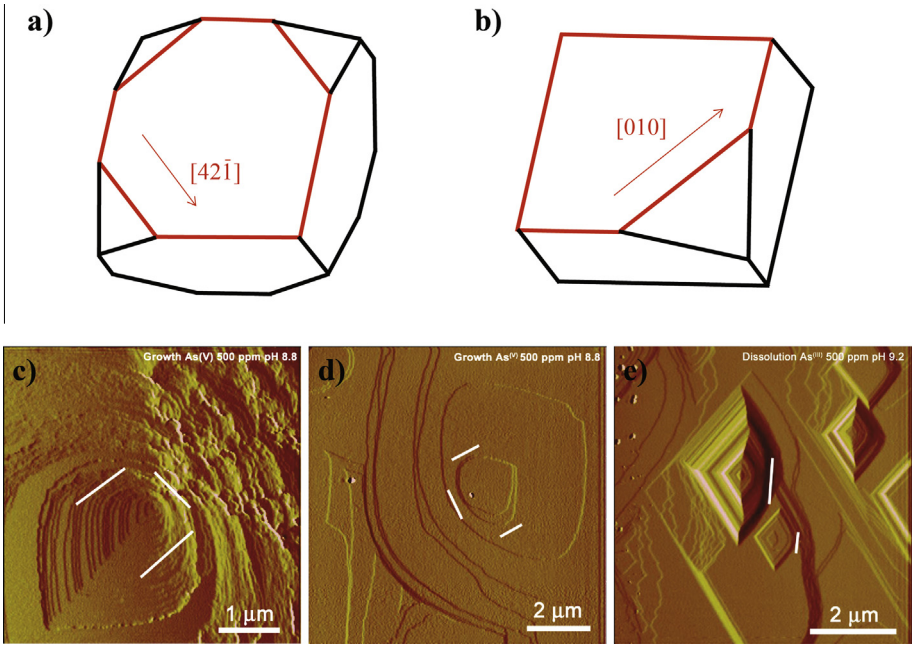

Fig. 9. Simulation of the calcite morphology with overdevelopment of the (a) {0112} and (b) {0001} forms. New edges develop, intersecting the typical rhombohedra shape of the growth and dissolution features. Examples of (c) growth hillocks, (d) growth islands and (e) etch pits showing new edges consistent with those developed in morphology simulations (marked with white lines).

stabilize hydration water by electrostatic interactions. At pH 5–6, 100% of $As^{(III)}$ is in the form of H_3AsO_3, and thus no interaction is expected. However, at the same pH, already 87 to 98% of $As^{(V)}$ is in the form of $H_2AsO_4^-$, and thus able to interact with the surface and stabilize hydration water even at this low pH. At pH 9.2, equal proportions of H_3AsO_3 and $H_2AsO_3^-$ are present in solution, and thus, this would explain why some effect in etch pit morphology is observed in dissolution experiments performed at pH 9.2 in the presence of $As^{(III)}$ at 500 ppm. At pH 11, around 10% of $As^{(III)}$ is present in the form of $HAsO_3^{2-}$ in the solution and interacts with the surface at high concentration of 500 ppm, modifying the etch pits geometry during dissolution and islands during growth.

4.2. Precipitation process during the interaction of dissolving calcite surfaces with arsenic-bearing aqueous solutions

Interestingly, at high $As^{(V)}$ concentration, a new precipitate forms during calcite dissolution, similar to that already observed for the dissolution of calcite in the presence of selenium (Putnis et al., 2013). Similarly, the precipitation of a calcium-arsenic phase while dissolving gypsum was observed by Rodríguez-Blanco et al. (2007). Calcium-arsenic precipitates were also reported in batch reactor experiments by Bothe and Brown (1999).

To explain our observations, PHREEQC simulations of the solution composition and saturation state with respect to relevant Ca-arsenate phases upon eventual equilibration with respect to the calcite substrate were performed. The different Ca–As solid phases considered and their solubility products are reported in Table 5, where the results of the simulations are summarized. These results indicate that already at the lowest $As^{(V)}$ concentration tested here (5 ppm) the solution would be supersaturated with respect to pharmacolite, while it is undersaturated with respect to other Ca-arsenate phases. Note that this crude simulation is just an approximation as (i) the semi-continuous flow through the AFM cell will retard equilibration with respect to calcite; (ii) precipitation may occur from an interfacial fluid layer in contact with the solid, while the bulk solution may remain undersaturated (Ruiz-Agudo et al., 2012). Nevertheless, it illustrates that under these conditions, precipitation of an As-bearing phase is possible (as we observed in our experiments) and it is coupled to the dissolution of calcite which provides the calcium atoms necessary to form a new calcite-arsenic phase within the mineral-fluid interfacial boundary layer.

4.3. Implications and environmental relevance

The adsorption of arsenic on iron and aluminum oxides has been proposed as the main mechanism controlling the mobility of arsenic in soils and sediments and eventually its precipitation into arsenic phases. Adsorption depends on pH and oxidation state, with arsenate being more strongly adsorbed than arsenite (Carillo and Drever, 1998). Arsenate $As^{(V)}$ sorption was measured on calcite particles from a soil and shown to increase from pH 6–10, with a peak between pH 10 and 12, and decrease above pH 12 (Goldberg and Glaubig, 1988). The adsorption of $As^{(V)}$ on calcite was four times larger than on montmorillonite or kaolinite particles in the same soil. During the active precipitation of iron oxyhydroxides and carbonates associated with the oxygenation and CO_2 degassing of hydrothermal spring waters in the Cézallier area of the French Massif

Table 4
Equilibrium constants used in PHREQC calculations, compiled from Martínez-Villegas et al. (2013) and Nordstrom et al. (2014).

Name	Formula	Reaction	Log *K*
Solid phases			*Calcium arsenates*
Ferrarisite	$Ca_5H_2(AsO_4)_4{\cdot}9H_2O$	$Ca_5H_2(AsO_4)_4{:}9H_2O = 5Ca^{2+} + 2AsO_4^{2-} + 2HAsO_4^{-} + 9H_2O$	−31.49
Guerinite	$Ca_5H_2(AsO_4)_4{\cdot}9H_2O$	$Ca_5H_2(AsO_4)_4{:}9H_2O = 5Ca^{2+} + 2AsO_4^{2-} + 2HAsO_4^{-} + 9H_2O$	−30.69
Weilite	$CaHAsO_4$	$CaHAsO_4 + H^+ = Ca^{2+} + H_2AsO_4^-$	2.36
Haidingerite	$CaHAsO_4{\cdot}H_2O$	$CaHAsO_4{:}H_2O = Ca^{2+} + HAsO_4^{2-} + H_2O$	−4.79
Pharmacolite	$CaHAsO_4{\cdot}2H_2O$	$CaHAsO_4{:}2H_2O + H^+ = Ca^{2+} + H_2AsO_4^- + 2H_2O$	−4.68
Johnbaumite	$Ca_5(OH)(AsO_4)_3$	$Ca_5(OH)(AsO_4)_3 = 5Ca^{2+} + 3AsO_4^{3-} + OH^-$	−38.04
	$Ca_2(OH)(AsO_4){\cdot}2H_2O$	$Ca_2(OH)(AsO_4){:}2H_2O + H^+ = 2Ca^{2+} + AsO_4^{3-} + 3H_2O$	1.29
	$Ca_3(AsO_4)_2{\cdot}2.25H_2O$	$Ca_3(AsO_4)_2{:}2.25H_2O = 3Ca^{2+} + 2AsO_4^{3-} + 2.25H_2O$	−21.40
	$Ca_3(AsO_4)_2{\cdot}3H_2O$	$Ca_3(AsO_4)_2{:}3H_2O = 3Ca^{2+} + 2AsO_4^{3-} + 3H_2O$	−21.14
	$Ca_3(AsO_4)_2{\cdot}3.67H_2O$	$Ca_3(AsO_4)_2{:}3.67H_2O = 3Ca^{2+} + 2AsO_4^{3-} + 3.67H_2O$	−21.00
	$Ca_3(AsO_4)_2{\cdot}4H_2O$	$Ca_3(AsO_4)_2{:}4H_2O = 3Ca^{2+} + 2AsO_4^{3-} + 4H_2O$	−18.91
	$Ca_3(AsO_4)_2{\cdot}4.25H_2O$	$Ca_3(AsO_4)_2{:}4.25H_2O = 3Ca^{2+} + 2AsO_4^{3-} + 4.25H_2O$	−21.00
	$Ca_4(OH)_2(AsO_4)_2{\cdot}4H_2O$	$Ca_4(OH)_2(AsO_4)_2{:}4H_2O = 4Ca^{2+} + 2AsO_4^{3-} + 2OH^- + 4H_2O$	−29.20
Relevant aqueous complexes			
	$H_2AsO_4^-$	$H_3AsO_4 = H_2AsO_4^- + H^+$	−2.28
	$HAsO_4^{2-}$	$H_2AsO_4^- = HAsO_4^{2-} + 2\ H^+$	−6.96
	AsO_4^{3-}	$HAsO_4^{2-} = AsO_4^{3-} + 3H^+$	−11.58
	$H_2AsO_3^-$	$H_3AsO_3 = H_2AsO_3^- + H^+$	−9.23
	NaH_2AsO_4	$Na^+ + H_2AsO_4^- = NaH_2AsO_4$	1.78
	$NaHAsO_4^-$	$Na^+ + HAsO_4^{2-} = NaHAsO_4^-$	0.69
	$NaAsO_4^{2-}$	$Na^+ + AsO_4^{3-} = NaAsO4^{2-}$	4.71
	NaH_2AsO_3	$Na^+ + H_2AsO_3^- = NaH_2AsO_3$	0.25
	$CaH_2AsO_4^+$	$Ca^{2+} + H_2AsO_4^- = CaH_2AsO_4^+$	1.06
	$CaHAsO_4$	$Ca^{2+} + HAsO_4^{2-} = CaHAsO_4$	2.69
	$CaAsO_4^-$	$Ca^{2+} + AsO_4^{3-} = CaAsO_4^-$	6.22
	$CaH_2AsO_3^+$	$Ca^{2+} + H_2AsO_3^- = CaH_2AsO_3^+$	1.81

Table 5
Saturation indexes of different Ca–$As^{(V)}$ phases calculated with PHREEQC assuming equilibrium with respect to calcite, as a function of $As^{(V)}$ concentration at 25 °C.

Phase	SI (PHREEQC)		
	As^V (5 ppm)	As^V (50 ppm)	As^V (500 ppm)
Pharmacolite	**1.64**	**4.19**	**5.78**
Haidingerite	−5.04	−2.49	−0.90
Weilite	−5.4	−2.85	−1.26
$Ca_3(AsO_4)_2{\cdot}2.25H_2O$	−6.07	−3.01	−1.6
$Ca_3(AsO_4)_2{\cdot}3H_2O$	−6.33	−3.27	−1.86
$Ca_3(AsO_4)2{\cdot}3.67H_2O$	−6.47	−3.41	−2.00
$Ca_3(AsO_4)_2{\cdot}4.25H_2O$	−6.47	−3.41	−2.00
Ferrarisite	−15.65	−7.49	−2.89
Guerinite	−16.45	−8.29	−3.69
$Ca_3(AsO_4)_2{\cdot}4H_2O$	−8.56	−5.5	−4.09
Johnbaumite	−9.50	−5.92	−4.69
$Ca_2(OH)(AsO_4){\cdot}2H_2O$	−7.35	−6.83	−7.02
$Ca_4(OH)_2(AsO_4)_2{\cdot}4H_2O$	−10.94	−9.92	−10.28

The supersaturation of the pharmacolite at all arsenic concentrations is indicated in bold values.

Central, arsenic interacted preferentially with iron oxides (Le Guern et al., 2003). These authors suggested that calcite plays only a minor role in arsenic trapping when iron oxides are present.

Arsenic may either adsorb on calcite crystals or be incorporated during calcite growth. In the past 15 years, a large body of experimental data has shown that both processes may occur. However, some results regarding the net incorporation of $As^{(III)}$ and $As^{(V)}$ into calcite are still debated. Our study shows that the effects of arsenic on calcite growth and dissolution are observed for high concentrations (above 50 ppm) in short-term experiments, conditions that are rarely met under natural conditions. However, high concentrations of arsenic can be reached during anthropogenic activity, such as acid mine drainage, and high arsenic concentrations might affect calcite growth and dissolution in the short-term during soil irrigation with highly contaminated water in calcareous environments.

Finally, the incorporation of arsenic in calcite is potentially important since many arsenic affected groundwaters are at equilibrium or slightly supersaturated with respect to calcite and in several natural carbonate systems iron oxides are absent. Natural calcite minerals may be in contact with contaminated ground water and streams or with acid mine drainage flows. As a consequence, calcite represents a key mineral to understand the global cycling of arsenic into the environment.

5. CONCLUSION

In situ atomic force microscopy measurements of the interactions between calcite and arsenic-bearing solutions in the pH range 6–11, complemented by ex situ XAS characterization of nanocalcite grown in the presence of arsenic oxyanions in the pH range 6–11, lead to the following conclusions.

1. The AFM results, supported by EXAFS measurements, show that As(V) is (i) partly adsorbed during growth, this causing the effects observed on step morphology, and (ii) partly incorporated, this possibly causing change in growth from rhombohedral to tear-shaped growth spirals.
2. During growth, the effect of As(III) is much less because it is weakly incorporated and changes the morphology of the steps only at high concentrations (500 ppm). XANES measurements show that As(III) may be incorporated during calcite growth and partly oxidized, leading to nanocalcite particles containing 34% As(III) and 66% As(V).
3. During dissolution, arsenic is adsorbed on the calcite surface, changing the morphology of etch pits and roughening the whole surface, and increasing the kinetics of dissolution. At the highest concentration (500 ppm of As(V)), calcite dissolution is coupled to the precipitation of a calcium arsenate phase.
4. An interpretation is proposed where the polarity of the calcite steps control the adsorption of the various arsenic oxyanions.
5. More studies would be necessary to characterize the relative proportion of adsorbed versus incorporated arsenic concentrations in calcite.

ACKNOWLEDGEMENTS

The authors thank V. Rapelius for help with ICP-OES analyses at Münster University, S. Bureau for the help with ICP-AES analyses at ISTerre, and O. Proux for the XAS measurements performed on the beamline FAME at ESRF. The experimental facilities in the Institut für Mineralogie, University of Münster, are supported by the German Research Council (DFG). E. Ruiz-Agudo acknowledges the receipt of a Ramón y Cajal grant from Spanish Ministry of Economy and Competitiveness, as well as additional funding from the Spanish Government (grant MAT2012-37584-ERDF funds) and the Junta de Andalucía (research group RNM-179 and project P11-RNM-7550). Funding from Labex OSUG@2020 (Investissement d'avenir-ANR10-LABX56) and Labex Serenade are acknowledged. We thank Alejandro Fernandez-Martinez for fruitful discussions.

APPENDIX A. SUPPLEMENTARY DATA

Supplementary data associated with this article can be found, in the online version, at http://dx.doi.org/10.1016/j.gca.2015.03.025.

REFERENCES

Alexandratos V. G., Elzinga E. J. and Reeder R. J. (2007) Arsenate uptake by calcite: macroscopic and spectroscopic characterization of adsorption and incorporation mechanisms. *Geochim. Cosmochim. Acta* **71**, 4172–4187.

Aurelio G., Fernandez-Martinez A., Cuello G. J., Roman-Ross G., Alliot I. and Charlet L. (2010) Structural study of selenium(IV) substitutions in calcite. *Chem. Geol.* **270**, 249–256.

Ayotte J. D., Montgomery D. L., Flanagan S. M. and Robinson K. W. (2003) Arsenic in groundwater in eastern New England: occurrence, controls, and human health implications. *Environ. Sci. Technol.* **37**, 2075–2083.

Baerup L. A., Navarre-Sitchler A. K., Maxwell R. M. and McCray J. E. (2012) Kinetic metal release from competing processes in aquifers. *Environ. Sci. Technol.* **46**, 6539–6547.

Bardelli F., Benvenuti M., Costagliola P., Di Benedetto F., Lattanzi P., Meneghini C., Romanelli M. and Valenzanon L. (2011) Arsenic uptake by natural calcite: an XAS study. *Geochim. Cosmochim. Acta* **75**, 3011–3023.

di Benedetto F., Costagliola P., Benvenuti M., Lattanzi P., Romanelli M. and Tanelli G. (2006) Arsenic incorporation in natural calcite lattice. Evidence from electron spin echo spectroscopy. *Earth Planet. Sci. Lett.* **246**, 458–465.

Bothe, Jr., J. V. and Brown P. W. (1999) The stabilities of calcium arsenate at 23 ± 1°C. *J. Hazard. Mater.* **B69**, 197–207.

Bowell R. J. and Parshley J. V. (2005) Control of pit-lake water chemistry by secondary minerals, Summer Camp Pits, Getchell mine, Nevada. *Chem Geol.* **215**, 373–385.

Carillo A. and Drever J. I. (1998) Adsorption of arsenic by natural aquifer material in the San Antonio-El Triunfo mining area, Baja California, Mexico. *Environ. Geol* **35**, 251–257.

Charlet L., Chakraborty S., Appelo C. A. J., Román-Ross G., Nath B., Ansari A. A., Lanson M., Chatterjee D. and Basu Mallik S. (2007) Chemodynamics of an arsenic "hotspot" in a West Bengal aquifer: A field and reactive transport modeling study. *Appl. Geochem.* **22**, 1273–1292.

Cheng L., Fenter P., Sturchio N. C., Zhong Z. and Bedzyk M. J. (1999) X-ray standing wave study of arsenite incorporation at the calcite surface. *Geochim. Cosmochim. Acta* **63**, 3153–3157.

Christen K. (2001) The arsenic threat worsens. *Environ. Sci. Technol.* **35**, 286A–291A.

Costagliola P., Bardelli F., Benvenuti M., Di Benedetto F., Lattanzi P., Romanelli M., Paolieri M., Rimondi V. and Vaggelli G. (2013) Arsenic-bearing calcite in natural travertines: evidence from sequential extraction, XAS and XRF. *Environ. Sci. Technol.* **47**, 6231–6238.

Cullen W. R. and Reimer K. J. (1989) Arsenic speciation in the environment. *Chem. Rev.* **89**, 713–764.

Davis K. J., Dove P. M. and De Yoreo J. J. (2000) The role of Mg^{2+} as an impurity in calcite growth. *Science* **290**, 1134–1137.

Dove P. M. and Hochella, Jr., M. F. (1993) Calcite precipitation mechanisms and inhibition by orthophosphate: in situ observations by scanning force microscopy. *Geochim. Cosmochim. Acta* **57**, 705–714.

Frost R. L., Bahfenne S., Čejka J., Sejkora, Plášil J. and Palmer S. J. (2010) Raman spectroscopic study of the hydrogen–arsenate mineral pharmacolite $Ca(AsO_3OH)\cdot 2H_2O$ – implications for aquifer and sediment remediation. *J. Raman Spectrosc.* **41**, 1348–1352.

Gentzis T., Goodarzi F. and Foscolos A. E. (1997) Geochemistry and mineralogy of Greek lignites from the Ioannina basin. *Energy Sources* **19**, 111–128.

Goldberg S. and Glaubig R. A. (1988) Anion sorption on a calcareous, montmorillonitic soil – arsenic. *Soil Sci. Soc. Am. J.* **52**, 1297–1300.

Guo H., Zhang D., Wen D., Wu Y., Ni P., Jiang Y., Guo Q., Li F., Zheng H. and Zhou Y. (2014) Arsenic mobilization in aquifers of the southwest Songnen basin, PR China: evidences from chemical and isotopic characteristics. *Sci. Total Environ.* **490**, 590–602.

Horton T. W., Becker J. A., Craw D., Koons P. O. and Page Chamberlain C. (2001) Hydrothermal arsenic enrichment in an active mountain belt, Southern Alps, New Zealand. *Chem. Geol.* **177**, 323–339.

Julliot F., Ildefonse P., Morin G., Calas G., Kersabiec A. M. and Benedetti M. (1999) Remobilization of arsenic from buried wastes at an industrial site: mineralogical and geochemical control. *Appl. Geochem.* **14**, 1031–1048.

Kim M. J., Nriagu J. and Haack S. (2000) Carbonate ions and arsenic dissolution by groundwater. *Environ. Sci. Technol.* **34**, 3094–3100.

Larsen K., Bechgaard K. and Stipp S. L. S. (2010) The effect of the Ca^{2+} to CO_3^{2-} activity ratio on spiral growth in the calcite $\{10\bar{1}4\}$ surface. *Geochim. Cosmochim. Acta* **74**, 2099–2109.

Le Guern C., Baranger P., Crouzet C., Bodénan F. and Conil P. (2003) Arsenic trapping by iron oxyhydroxides and carbonates at hydrothermal spring outlets. *Appl. Geochem.* **18**, 1313–1323.

Martínez-Villegas N., Briones-Gallardo R., Ramos-Leal J. A., Avalos-Borja M., Castañón-Sandoval A. D., Razo-Flores E. and Villalobos M. (2013) Arsenic mobility controlled by solid calcium arsenates: a case study in Mexico showcasing a potentially widespread environmental problem. *Environ. Pollut.* **176**, 114–122.

Montes-Hernandez G., Renard F., Geoffroy N., Charlet L. and Pironon J. (2007) Calcite precipitation from CO_2-H_2O-$Ca(OH)_2$ slurry under supercritical and gas CO_2 media. *J. Cryst. Growth* **308**, 228–236. http://dx.doi.org/10.1016/jcrysgro.2007.08.005.

Montes-Hernandez G., Concha-Lozano N., Renard F. and Quirico E. (2009) Removal of oxyanions from synthetic wastewater via carbonation process of calcium hydroxide: fundamentals and applications. *J. Hazard. Mater.* **166**, 788–795.

Montes-Hernandez G., Sarret G., Hellmann R., Menguy N., Testemale D., Charlet L. and Renard F. (2011) Nanostructured calcite precipitated under hydrothermal conditions in the presence of organic and inorganic selenium. *Chem. Geol.* **290**, 109–120.

Montes-Hernandez G., Renard F. and Lafay R. (2013) Experimental assessment of CO_2–mineral–toxic ion interactions in a simplified freshwater aquifer: Implications for CO_2 leakage from deep geological storage. *Environ. Sci. Technol.* **47**, 6247–6253.

Nordstrom D. K., Majzlan J. and Königsberger E. (2014) Thermodynamic properties for arsenic minerals and aqueous species. *Rev. Miner. Geochem.* **79**, 217–255.

Ondrus P., Veselovsky F., Hlousek J., Skala R., Vavrin I., Fryda J., Cejka J., Gabasova A., Ondrus P., Veselovsky F., Hlousek J., Skala R., Vavrin I., Fryda J., Cejka J. and Gabasova A. (1997) Secondary minerals of the Jachymov (Joachimsthal) ore district. *J. Czech Geol. Soc.* **42**, 3–76.

Parkhurst D. L. and Appelo C. A. J. (1999) *Users guide to PHREEQC (version 2) a computer program for speciation, batch reaction, one dimensional transport and inverse geochemical calculations, Water-Resources Investigation report 99–4259*. U.S. Geological Survey, Washington, DC, p. 312.

Paquette J. and Reeder R. J. (1995) Relationship between surface structure, growth mechanism, and trace element incorporation in calcite. *Geochim. Cosmochim. Acta* **59**, 735–749.

Pierrot R. (1964) Contribution à la minéralogie des arséniates calciques et calcomagnésiens naturels. *Bull. Soc. franç. Minér. Crist.* **88**, 169–211.

Proux O., Nassif V., Prat A., Ulrich O., Lahera E., Biquard X., Menthonnex J.-J. and Hazemann J. L. (2005) Feedback system of a liquid-nitrogen-cooled double-crystal monochromator: design and performances. *J. Synchrotr. Radiat.* **13**, 59–68.

Putnis A. (2009) Mineral replacement reactions. *Rev. Mineral. Geochem.* **70**, 87–124.

Putnis C. V., Renard F., King H., Montes-Hernandez G. and Ruiz-Agudo E. (2013) Sequestration of selenium on calcite surfaces revealed by nanoscale imaging. *Environ. Sci. Technol.* **47**, 13469–13476.

Ravel B. and Newville M. (2005) ATHENA and ARTEMIS: interactive graphical data analysis using IFEFFIT. *Phys. Scripta* **T115**, 1007.

Renard F., Montes-Hernandez G., Ruiz-Agudo E. and Putnis C. V. (2013) Selenium incorporation into calcite and its effect on crystal growth process: An Atomic Force Microscopy study. *Chem. Geol.* **340**, 151–161.

Rimstidt J. D., Balog A. and Webb J. (1998) Distribution of trace elements between carbonate minerals and aqueous solutions. *Geochim. Cosmochim. Acta* **62**(11), 1851–1863.

Rodríguez-Blanco J. D., Jimenez A. and Prieto M. (2007) Oriented overgrowth of pharmacolite ($CaHAsO_4\cdot 2H_2O$) on gypsum ($CaSO_4\cdot 2H_2O$). *Cryst. Growth Des.* **7**, 2756–2763.

Rodrìguez-Lado L., Sun G., Berg M., Zhang Q., Xue H., Zheng Q. and Johnson C. A. (2013) Groundwater arsenic contamination throughout China. *Science* **241**, 866–868.

Román-Ross G., Cuello G. J., Turrillas X., Fernández-Martinez A. and Charlet L. (2006) Arsenite sorption and co-precipitation with calcite. *Chem. Geol.* **233**, 328–336.

Romero F. M., Armeinta M. A. and Carrillo-Chavez A. (2004) Arsenic sorption by carbonate-rich aquifer material, a control on arsenic mobility at Zimápan, México. *Arch. Environ. Contam. Toxicol.* **47**, 1–13.

Ruiz-Agudo E., Di Tommaso D., Putnis C. V., De Leeuw N. H. and Putnis A. (2010a) Interactions between organophosphonate-bearing solutions and (10$\bar{1}$4) calcite surfaces: an atomic force microscopy and first-principles molecular dynamics study. *Cryst. Growth Des.* **10**(7), 3022–3035.

Ruiz-Agudo E., Kowacz M., Putnis C. V. and Putnis A. (2010b) The role of background electrolytes on the kinetics and mechanism of calcite dissolution. *Geochim. Cosmochim. Acta* **74**, 1256–1267.

Ruiz-Agudo E., Putnis C. V., Wang L. and Putnis A. (2011) Specific effects of background electrolytes on the kinetics of step propagation during calcite growth. *Geochim. Cosmochim. Acta* **75**, 3803–3814.

Ruiz-Agudo E., Putnis C. V., Rodriguez-Navarro C. and Putnis A. (2012) Mechanism of leached layer formation during chemical weathering of silicate minerals. *Geology* **40**(10), 947–950.

Ruiz-Agudo E. and Putnis C. V. (2012) Direct observations of mineral-fluid reactions using atomic force microscopy: the specific example of calcite. *Mineral. Mag.* **76**, 227–253.

Simon G., Huang H., Penner-Hahn J. E., Kesler S. E. and Kao L.-S. (1999) Oxidation state of gold and arsenic in gold-bearing arsenian pyrite. *Am. Mineral.* **84**, 1071–1079.

Song S., Lopez-Valdivieso A., Hernandez-Campos D. J., Peng C., Monroy-Fernandez M. G. and Razo-Soto I. (2006) Arsenic removal from high-arsenic water by enhanced coagulation with ferric ions and coarse calcite. *Water Res.* **40**, 364–372.

Stipp S. L. S., Christensen J. T., Lakshtanov L. Z., Baker J. A. and Waight T. (2006) Rare Earth element (REE) incorporation in natural calcite: upper limits for actinide uptake in a secondary phase. *Radiochim. Acta* **94**, 523–528.

Sø H. U., Postma D., Jakobsen R. and Larsen F. (2008) Sorption and desorption of arsenate and arsenite on calcite. *Geochim. Cosmochim. Acta* **72**, 5871–5884.

Tabelin C. B., Hashimoto A., Igarashi T. and Yoneda T. (2014) Leaching of boron, arsenic and selenium from sedimentary rocks: II. pH dependence, speciation and mechanisms of release. *Sci. Total Environ.* **473–474**, 244–253.

Vansant F. K., van der Veken B. J. and Desseyn H. O. (1973) Vibrational analysis of arsenic acid and its anions I: description of the Raman spectra. *J. Mol. Struct.* **15**, 425–437.

Ward C. R., Spears D. A., Booth C. A., Station I. and Gurba L. W. (1999) Mineral matter and trace elements in coals of the Gunnedah Basin, New South Wales, Australia. *Int. J. Coal Geol.* **40**, 281–308.

Wang L., Ruiz-Agudo E., Putnis C. V. and Putnis A. (2011) Direct observations of the modification of calcite growth morphology by Li^+ through selectively stabilizing an energetically unfavourable face. *CrystEngComm* **13**(12), 3962–3966.

Wells J. D. and Mullens T. E. (1973) Gold-bearing arsenian pyrite determined by microprobe analysis, Cortez and Carlin gold mines, Nevada. *Econ. Geol.* **68**, 187–201.

Winkel L. H. E., Casentini B., Bardelli F., Voegelin A., Nikolaidis N. P. and Charlet L. (2013) Speciation of arsenic in Greek travertines: co-precipitation of arsenate with calcite. *Geochim. Cosmochim. Acta* **106**, 99–110.

Wunsch A., Navarre-Sitchler A. K., Moore J. and McCray J. E. (2014) Metal release from limestones at high partial-pressures of CO_2. *Chem. Geol.* **363**, 40–55.

Yokoyama Y., Mitsunobu S., Tanaka K., Itai T. and Takahashi Y. (2009) A study on the coprecipitation of arsenite and arsenate into calcite coupled with the determination of oxidation states of arsenic both in calcite and water. *Chem. Lett.* **38**, 910–911.

Yokoyama Y., Tanaka K. and Takahashi Y. (2012) Differences in the immobilization of arsenite and arsenate by calcite. *Geochim. Cosmochim. Acta* **91**, 202–219.

Zheng Y., Stute M., van Geen A., Gavrieli I., Dhar R., Simpson H. J., Schlosser P. and Ahmed K. M. (2004) Redox control of arsenic mobilization in Bangladesh groundwater. *Appl. Geochem.* **19**, 201–214.

Associate editor: Mario Villalobos